Single-step, High Pressure, and Two-Step Spark Plasma Sintering of UO2 nanopowders

E. de Bona, L. Balice, L. Cognini, M. Holzhäuser, K. Popa, O. Walter, M. Cologna, D. Prieur, T. Wiss, Gianguido Baldinozzi

Journal Pre-proof

Single-step, High Pressure, and Two-Step Spark Plasma Sintering of UO_2 nanopowders

E. De Bona, L. Balice, L. Cognini, M. Holzhäuser, K. Popa, O. Walter, M. Cologna, D. Prieur, T. Wiss, G. Baldinozzi

PII: S0955-2219(21)00022-4

DOI: https://doi.org/10.1016/j.jeurceramsoc.2021.01.020

Reference: JECS 13833

To appear in: *Journal of the European Ceramic Society*

Received Date: 19 August 2020

Revised Date: 8 January 2021

Accepted Date: 9 January 2021

Please cite this article as: De Bona E, Balice L, Cognini L, Holzhäuser M, Popa K, Walter O, Cologna M, Prieur D, Wiss T, Baldinozzi G, Single-step, High Pressure, and Two-Step Spark Plasma Sintering of UO_2 nanopowders, *Journal of the European Ceramic Society* (2021), doi: https://doi.org/10.1016/j.jeurceramsoc.2021.01.020

Single-step, High Pressure, and Two-Step Spark Plasma Sintering of UO_2 nanopowders

De Bona E.[1,2]*, Balice L.[3,4], Cognini L.[1,5], Holzhäuser M.[1], Popa K.[1], Walter O.[1], Cologna M.[1]*, Prieur D.[6], Wiss T.[1], Baldinozzi G.[2]

[1]European Commission, Joint Research Centre (JRC), Postfach 2340, 76125 Karlsruhe, Germany
[2]Laboratoire Structures, Propriétés et Modélisation des Solides, CNRS, CentraleSupélec, Université Paris-Saclay, 91190 Gif-sur-Yvette, France
[3]Université Grenoble Alpes, 621 Avenue Centrale, 38400 Saint-Martin-d'Hères, France
[4]CEA, DEN, CAD, DEC, F-13108 Saint-Paul-lez-Durance Cedex, France
[5]Politecnico di Milano, Department of Energy, Nuclear Engineering Division, via La Masa 34, I-20156 Milano, Italy
[6]Helmholtz-Zentrum Dresden-Rossendorf, Institute of Resource Ecology, 01328 Dresden, Germany

First author's current address/affiliation: Helmholtz-Zentrum Dresden-Rossendorf, Institute of Resource Ecology, 01328 Dresden, Germany

*Corresponding author(s) at: European Commission, Joint Research Centre (JRC), Karlsruhe, Germany
Marco.COLOGNA@ec.europa.eu (M. Cologna)
Emanuele.DE-BONA@ext.ec.europa.eu (E. De Bona)

Abstract

Three different Spark Plasma Sintering (SPS) treatments were applied to highly sinteractive, near-stoichiometric $UO_{2.04}$ nanocrystalline (5 nm) powders produced by U(IV) oxalate hydrothermal decomposition at 170 °C. The sintering conditions for reaching 95 % Theoretical Density (TD) in regular SPS, high pressure SPS (HP-SPS), and, for the first time, two-step SPS (2S-SPS), were determined. Densification to 95 % TD was achieved at 1000 °C in regular SPS (70 MPa applied pressure), 660 °C in HP-SPS (500 MPa), and 650-550 °C in 2S-SPS (70 MPa). With the goal of minimising the grain growth during densification, the sintering treatments were optimised to favour densification over coarsening, and the final microstructures thus obtained are compared. Equally dense UO_2 samples of different grain sizes, ranging from 3.08 µm to 163 nm, were produced. Room-temperature oxidation of the powders could not be avoided due to their nanometric dimensions, and a final annealing treatment was designed to reduce hyperstoichiometric samples to $UO_{2.00}$.

Keywords: Spark Plasma Sintering; Uranium Dioxide; Microstructure; Coarsening; Two Step Sintering

1 Introduction

During reactor operation, oxide nuclear fuels undergo deep microstructural and chemical modifications that transform the fresh fuel into spent nuclear fuel (SNF). While nuclear fissions, radioactive decays and neutron captures change the chemical composition, the high temperatures, radiation damage, and gas production transform the microstructure. Due to the higher neutron flux[1] at the rim of the fuel pellets, the so-called high burnup structure (HBS) develops after long-term

operation, with the reorganisation of the initial 10-15 µm grains into a pattern of smaller ones of 100-300 nm surrounding micrometric pores[2–6]. The formation of this region rich of grain boundaries was found to slightly reduce the degradation of the overall properties of the fuel, for example in terms of thermal conductivity or fission gas retention[6–8]. For the understanding of the fuel performance during irradiation but also in view of its interim storage or final disposal, it is fundamental to understand the behaviour of the HBS, most of all due to its peripheric position: in case of failure of the confinement, this will be the first interface of the fuel towards external environment. In nominal operating conditions it is the phase at the interface with the cladding where the thermal and mechanical characteristics are also fundamental.

However, the study of real SNF is extremely cumbersome, due to the above-mentioned complexities and the high radiotoxicity of some of the isotopes generated during irradiation in the reactor. A solution to this problem is the use of surrogate systems (SIMFUEL) mimicking one of the features of real SNF, allowing the study of a simpler problem, and reducing the risk for the operators.

While some effort was put into reproducing the chemical composition of SNF[9–11], the HBS was not correctly mimicked yet. Due to the high temperatures (1600-1800 °C) and holding times (3-6 h) involved in conventional sintering of UO_2[12], densification is always accompanied by coarsening, resulting into the typical grain size of 10-15 µm of commercial fuel[13]. More recently, the development of techniques like Spark Plasma Sintering (SPS) significantly lowered the sintering temperatures and hold times, paving the way for the synthesis of compounds with reduced grain sizes that were inaccessible until then[14,15]. SPS was indeed successfully used for the inclusion of volatile fission products (FP) in the SIMFUEL[16,17], as well as for the production of UO_2, UO_{2+x}, and ThO_2 with submicrometric grain size[18–23].

In this work, aiming at reproducing the typical HBS grain size, three different SPS methods were compared: (i) conventional SPS (hereafter also called single-step SPS), (ii) high-pressure SPS (HP-SPS), and (iii) two-step SPS (2S-SPS). In HP-SPS the replacement of the graphite die and punches with SiC components allowed raising the applied pressure from 100 to 500 MPa. This provided extra driving force to the densification, lowering the sintering temperature while limiting coarsening, and thus resulted into a finer final microstructure in the sintered material[19–23].

Two-step spark plasma sintering was performed with the standard graphite SPS setup. This technique involves the quick firing of the green pellet at a higher temperature (T_1) to achieve intermediate density, after which the sample is cooled down and held for a long time at a lower temperature (T_2), where densification is completed[24]. Two-step sintering takes advantage of the different activation energies for grain boundary diffusion and grain boundary migration, and with the right choice of T_1 and T_2 grain growth is inhibited in the second sintering stage. To achieve this, the density reached in the first step must be above 75 % TD, implying a sufficient number of triple-point junctions is already formed. These triple-point junctions will be pinning the grain boundaries in the following dwell step at T_2, while densification will proceed thanks to grain boundary diffusion. This approach, applied to conventional sintering, was successfully used to produce several nanograined ceramics[25–28], but was exploited only very limitedly for the densification of nuclear fuels. In the only work, 95 % TD UO_2 with 0.9 µm grain size was sintered at 1410-1310 °C, requiring a density above 85 % TD to be reached after the step at T_1[29]. The application of two-step sintering to SPS was used for the production of nanostructured TiO_2[30] and YSZ[31], but has not been extensively explored yet.

In this article, we report on the application of single-step SPS, HP-SPS, and two-step SPS to sinter UO_{2+x} nanopowders prepared by decomposition of uranium oxalate. Both thermal as well as hydrothermal decomposition of the oxalate were tested. Near-stoichiometric nanocrystalline UO_2 can

be produced with a simple heat treatment under Ar (thermal decompositions), during which the oxalate first dehydrates and amorphises below 300 °C, and then UO_2 starts crystallising around 400 °C[32]. However, in this way, the initial stacked-platelets structure of the oxalate is preserved as agglomerate in the oxide nanopowder, affecting its sintering behaviour and the final microstructure of the sintered material[33–35]. In order to improve the sinterability of the powders, the hydrothermal decomposition was preferred. In this synthesis route, the oxalate is heated in an autoclave in presence of water, and cuboid agglomerates are disassembled thanks to the transport of material in aqueous medium[36–38]. The shape of the resulting oxide agglomerates can be tuned by controlling the pH during the reaction[39].

A drawback of working with such nanosized and highly reactive powders is that they are prone to fast oxidation. This can be an issue in the SIMFUEL production, since the thermal conductivity of UO_2 significantly decreases for small deviations from stoichiometry[40,41], and hence Light Water Reactor (LWR) fuel has to maintain a very carefully controlled O/M ratio of 2.00[12,42]. An advantage of SPS in UO_2 processing is the naturally reductive environment developed by the graphite components, at temperatures above 600 °C[43]. By properly choosing the SPS sintering parameters, the starting hyperstoichiometric powder can be reduced to $UO_{2.00}$ during densification[14]. However, the insertion of SiC components in the HP-SPS setup partially hinders this reductive capability, resulting into slightly hyperstoichiometric sintered disks. Therefore, a further annealing treatment under reducing conditions is required[22].

SPS treatments were optimised to limit the maximum sintering temperature and hence control the coarsening in the final microstructure. For the first time, the two-step sintering (2S-SPS) of UO_2 was performed in SPS, allowing reduction to $UO_{2.00}$ and densification (95 % TD) at temperatures as low as 650-550 °C, and resulting into an average grain size of 478 ± 17 nm. Further improvement was achieved with the high pressure (HP-SPS) setup, by which densification was achieved at 660 °C with a grain size of 163 ± 9 nm. All samples were reduced to $UO_{2.00}$ after an annealing treatment at 600 °C for 2 h under Ar-4%H_2, while their microstructure was unaffected. Such a set of identical UO_2 samples, differing only by the grain size, will allow parametric studies on grain boundaries effect in UO_2, as well as serve as starting point for better mimicking in SIMFUELs the grain boundary density characteristic of the HBS microstructure.

2 Experimental part

2.1 Powder synthesis: hydrothermal decomposition of U(IV) oxalate

Considering the higher stability of U(IV) in the oxalate form, compared to the quick oxidation of UO_2 nanopowders, it was decided to store the U(IV) as oxalate and convert it into UO_2 only in small amounts for immediate usage, within few days in order to prevent excessive oxidation. For the hydrothermal decomposition route, batches of roughly 1 g of UO_2 nanopowder were synthesised by loading in an autoclave 2 g of oxalate, 5 mL of water, and 0.5 mL of hydrazine and heating up to 170 °C for 5 h under autogenic pressure. The precipitates were washed with water, ethanol, and acetone, and then dried for about 36 h in a desiccator at low pressure and under Ar flux.

The thermal decomposition was performed by heating 1 g of oxalate at 600 °C for 2 h under Ar flow (200 °C/h heating / cooling rate).

2.2 Powder densification: Spark Plasma Sintering

UO_2 powders were sintered into dense disks using an FCT Systeme GmbH SPS modified for inclusion in a 1x1x1.5 m^3 Ar glovebox. The temperature was measured by a thermocouple located in the fixed lower punch of the compaction unit. The implementation of the system in a glovebox for handling radioactive powders was described by Tyrpekl et al[44].

In the case of single-step SPS and 2S-SPS, samples of about 250 mg of powder were loaded into graphite dies of 6 mm of internal diameter and pre-pressed under 17 MPa (0.5 kN). During the treatment, heating and cooling ramps were performed at 200 °C/min, and a pressure of 70 MPa (2 kN) was applied before heating the sample and released after the cooling. The regular SPS treatment consisted of a dwell of 10 min at 1600 °C. In the optimised 2S-SPS treatment a short dwell of 3 s was performed at T_1 = 650 °C, followed by a dwell of 100 min at T_2 = 550 °C. Several tests were performed to assess the best combination of T_1 and T_2 in terms of final density, microstructure, and stoichiometry of the sintered disks. As shown in Table 1, 650-550 °C represents the best compromise between limiting the sintering temperature, achieving full reduction (to $UO_{2.00}$), and reaching a high level of densification (to 95 % TD). At lower temperatures the samples have O/M > 2.00; no significant decrease of the grain size was observed (only few tens of nm less), despite the significantly lower dwell temperature T_2. At even lower temperatures, samples became two-phased (UO_2 and U_4O_9, as detected by XRD), showing some regions with higher porosity and finer grains dispersed in a matrix with a coarser microstructure.

↓T_1 / T_2→	650 °C	600 °C	550 °C	500 °C	450 °C
700 °C					
650 °C				O/M > 2	
600 °C			O/M > 2	O/M > 2	
550 °C				Two-phase	Two-phase
500 °C					ρ < 95 % TD

Table 1: combination of T_1 and T_2 tested in 2S-SPS. Green boxes indicate 95 % TD $UO_{2.00}$ samples, yellow boxes indicate samples that densified up to 95 % TD but without undergoing full reduction, and orange boxes stand for samples that did not reach 95 % TD.

A higher pressure could be applied in the HP-SPS treatment thanks to SiC inserts (4 mm inner diameter) inside a modified graphite die, allowing exceeding the limit of 100 MPa imposed by the mechanical resistance of graphite. Schemes of the regular and HP-SPS setups are presented in Figure 1. Because of the reduced diameter and of the increased distance of the thermocouple from the sample, the mass of the powder was reduced to 150 mg, and the assessment of the sample temperature became more uncertain. A pressure of 500 MPa (6.3 kN) was applied to the samples during a 5 min dwell at 250 °C, and released at room temperature after cooling. Heating and cooling rates were reduced to 100 °C/min, and the samples were heated up to 660 °C and held at this temperature for 30 s. All the sintering parameters are summarised in Table 2. For 2S-SPS, the temperatures reported were the

lowest required to obtain high density (geometrical density ≥ 95 % TD) stoichiometric $UO_{2.00}$ after the dwell time. Higher sintering temperatures systematically produce larger grain size pellets.

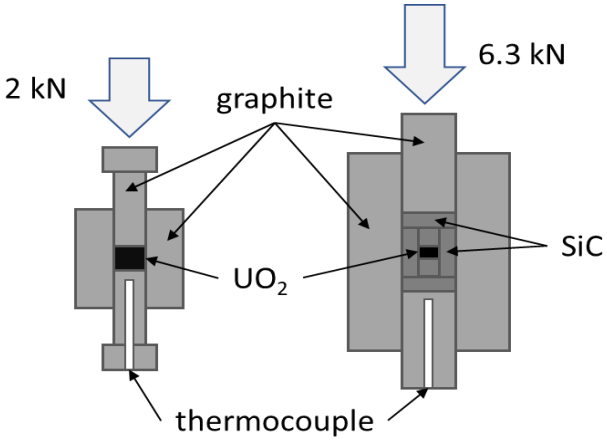

Figure 1: Schematic presentation of regular (left) and HP (right) SPS setups.

Treatment	σ [MPa]	T [°C]	t [min]	Ṫ [°C/min]
SPS	70	1600	10	200
2S-SPS	70	650-550	0.05-100	200
HP-SPS	500	660	0.5	100

Table 2: SPS treatments applied on the UO_2 nanopowders. SPS and 2S-SPS were performed in graphite dies, while in HP-SPS the powder was loaded into a SiC die.

As mentioned in the introduction, HP-SPS samples were not completely reduced to $UO_{2.00}$ after sintering. Therefore, all samples were annealed at 600 °C under Ar-H_2 for 2 h to reduce the stoichiometries to $UO_{2.00}$ without affecting the grain size.

2.3 Experimental characterisations

XRD measurements were performed using a Rigaku Miniflex 600 diffractometer in Bragg-Brentano configuration, equipped with a ceramic copper source (40 kV, 15 mA), without a primary monochromator but filtered to remove the Kβ emission line ($K\alpha_1$ = 1.5406 Å, $K\alpha_2$ = 1.5444 Å). The diffracted signal was measured by a Hy-Pix 400MF 2D HPAD detector. XRD samples were prepared by mechanical grinding in a paraffin suspension, and then poured onto low-background Si sample holders. The device instrumental function was calibrated using LaB_6 as reference material. Analyses of the diffraction patterns were performed using the software Jana2006[45] and using Pseudo – Voigt functions for modelling the peaks shape. Rietveld refinements were performed to determine the lattice parameter. The deviation *x* from stoichiometry in UO_{2+x} ($x \leq 0.22$) was calculated from the lattice constant *a* by applying the relation **a = 5.4705 – 0.132x**, proposed by Teske et al[46]. The crystallite size and the microstrain were estimated by applying the Williamson – Hall analyses[47].

SEM images were acquired with a dual-beam Focused Ion Beam (FIB) ThermoFisher Scientific (ex FEI™) Versa 3D SEM with Field Emission Gun (FEG) operated at 30 KeV. The grain size was evaluated with the intercept method according to the standard ASTM E112 – 12[48]. Lamellas of about 100 nm of thickness for TEM inspection were also prepared using this device.

TEM analyses were performed using a FEI™ Tecnai G2 microscope, equipped with a field emission gun. Selective area electron diffractions (SAED) were acquired covering micrometre size regions. The diffractions were analysed and the crystal structure confirmed using the ProcessDiffraction program[49].

3 Results and discussion

3.1 UO_2 nanopowders

Before sintering, the UO_2 nanopowders were characterised by means of XRD and SEM. As can be seen from the XRD pattern presented in Figure 2, the UO_2 powders produced by hydrothermal decomposition displayed very broad peaks, characteristic of a nanocrystalline material: the crystallite size calculated by applying the Williamson – Hall approach was 5 ± 1 nm.

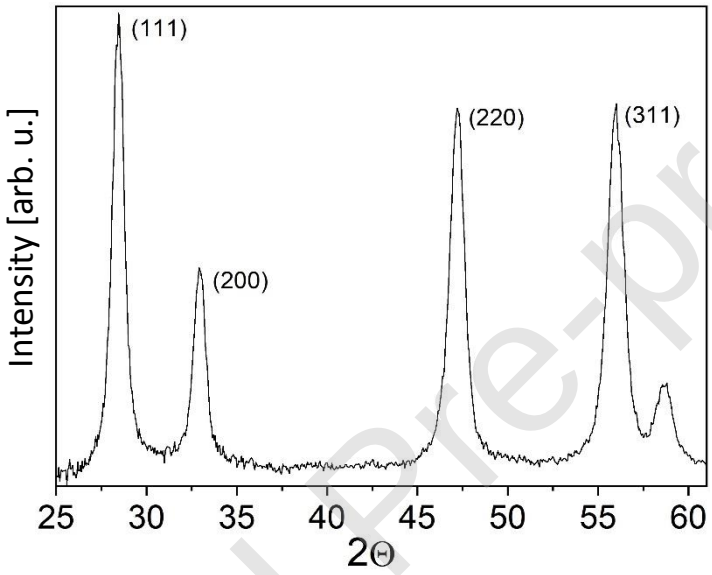

Figure 2: XRD pattern UO_2 nanopowders produced by hydrothermal decomposition.

Rietveld refinement of the pattern resulted in a lattice parameter of 5.464 ± 0.001 Å (goodness of fit GOF = 1.07, R-factor Rp = 8.84 %, weighed profile R-factor Rwp = 11.72 %), meaning an O/M ratio of 2.04.

Nevertheless, due to their nanometric size, these powders oxidised quickly also in the glovebox atmosphere (Ar or N_2, with N_2 possibly containing up to 1 % O_2 in certain moments). The oxidation of the powders over time was not studied in detail, but the O/M ratio increased up to 2.22 already after one week of storage in the glovebox. As storage time increases, further oxidation was detected from the lattice shrinkage, the changes in the peak shapes, and relative intensities changes (such as the ratio between the 002 and 220 reflections): these modifications are characteristic of the formation of U_4O_9 and U_3O_7[50]. However, when characterising such small crystalline domains with the setup used in this work, the peak broadening prevents the accurate quantitative determination of the relative amounts of U_4O_9 (and then U_3O_7) that were formed.

Deviation from stoichiometry increases the self-diffusion coefficients in UO_{2+x}[51], therefore increasing the sintering kinetics. However, such a quick oxidation is not desirable for the sake of reproducibility. Moreover, as mentioned in section 2.2, the HP-SPS setup does not involve the proper reduction of

hyperstoichiometric powders during sintering, resulting instead into biphasic UO_{2+x}-U_4O_9 pellets when sintering highly oxidised powders at lower temperatures.

The powder obtained by thermal decomposition of oxalate had a lattice parameter of 5.468 ± 0.001 Å (GOF = 1.09, Rp = 9.12 %, Rwp = 12.52 %), corresponding to an O/M ratio of 2.01, and crystallite size of 9 ± 1 nm.

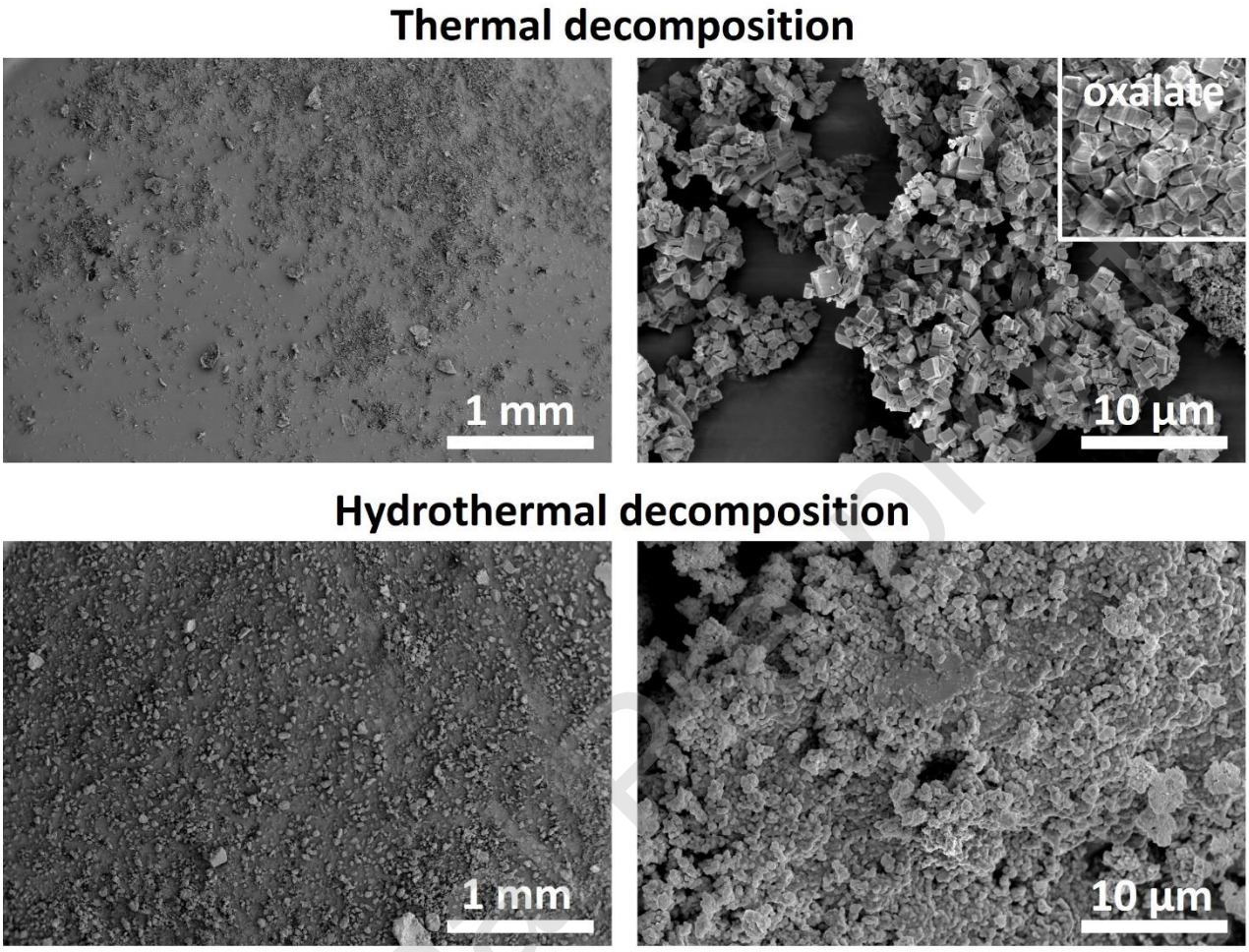

Figure 3: SEM SE pictures of the as-produced UO_2 nanopowders. The insert in the top right shows, at the same magnification, the initial U(IV) oxalate.

As shown in Figure 3, the hydrothermal decomposition was successful in disassembling the original oxalate microstructure (presented in the insert of Figure 3). By working with nearly neutral pH[39], the micron-sized cuboids of stacked platelets were replaced by small polycrystalline particles of about 200-300 nm of diameter, softly agglomerated into larger irregular lumps of 50-100 µm of size. The subsequent improvement of the powder sintering behaviour is reported in the following section.

3.2 Spark Plasma Sintering of the powders

SPS devices allow following and recording several parameters during the sintering treatment, revealing in real time the sintering behaviour of the powders. The most interesting parameter to follow is the relative displacement of the upper piston. In the reported data a positive displacement rate indicates shrinkage of the system which can be due to the densification of the sample, cooling or an increase of the applied pressure. A positive piston displacement rate instead signals the sample or piston expansion, for example during heating or while unloading the force.

A quantification of the actual densification of the powder is possible only upon correction of the piston displacement curve for thermal expansion and contribution of the graphite components. However, when comparing two treatments having the same setup and thermal schedule, the differences in the piston displacement can be attributed solely to the different powder behaviours. On the other hand, it is worth noting that the amplitude of the piston relative displacement depends also on the initial height of the sample, that is a function of the sample mass and green density (and therefore of the powder packing density and of the external applied pressure).

In this section, the piston displacement (and piston speed) as recorded by the device will be reported to qualitatively illustrate the different behaviours of the powders depending on the decomposition route and on the applied treatment. The final density of the samples was measured after the treatment, rather than calculated from the SPS parameters.

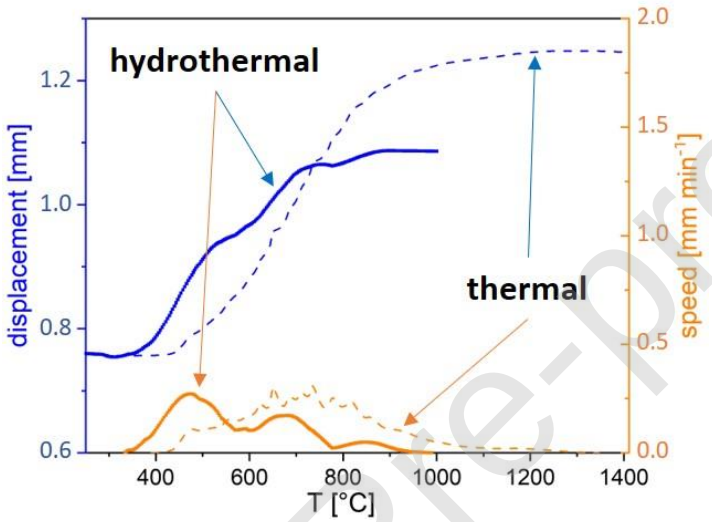

Figure 4: Piston displacement and speed during SPS of UO_2 powders derived from U(IV) oxalate by thermal (dotted line) and hydrothermal decomposition (full line).

Figure 4 shows the improvement in the SPS behaviour of the UO_2 nanopowders replacing the thermal decomposition with the hydrothermal route. The sintering part of the piston relative displacement and piston speed during the heating of the two powders in SPS are compared (the curves were cut after the sintering for the sake of simplicity). By disassembling the oxalate cuboids, sintering took place at lower temperatures, with the onset being shifted from around 420 °C to about 350 °C. More importantly, the end of the sintering also occurred at much lower temperatures, reduced from 1200 to 950 °C. This latter feature is the most important in terms of limiting the final grain size, as grain growth takes place predominantly at high temperatures and densities[52].

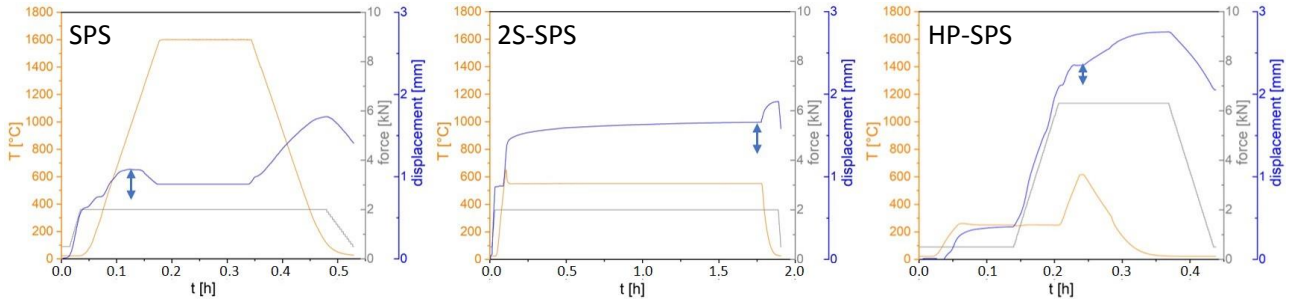

Figure 5: Temperature, applied force, and relative piston displacement as recorded by the machine during SPS, 2S-SPS, and HP-SPS of the UO_2 nanopowders. Sintering is highlighted by the small blue arrows on the piston displacement curves.

Figure 5 shows the sintering behaviour of the UO_2 nanopowder in the three different SPS treatments of this study. Measured temperatures and applied forces are also reported. Small blue arrows mark the sintering in each treatment, while the shrinkage recorded starting from 100 °C (not visible in the 2S-SPS treatment using this time scale), was attributed to the removal of residual H_2O adsorbed on the surface of the powder.

In the SPS treatment, a thermal expansion phase followed the sintering while heating, and the piston position did not change during the hold time at 1600 °C. In the frame of limiting the final grain size, these late stages are undesirable, as they do not contribute anymore to the densification of the sample while grain growth can take place.

Therefore, in the 2S-SPS treatment, the heating ramp was stopped before reaching the full densification (650 °C instead of about 900 °C), that was then completed very slowly (100 min) at a lower temperature (550 °C). In the last part of the dwell, the piston displacement proceeds extremely slowly until eventually stopping when the densification process was completed (at this low temperature, contributions from graphite creep can be ruled out). With the appropriate choice of the sintering parameters, the density of three-points junctions generated in the first quick heating should be high enough to pin grain boundaries, preventing grain growth while allowing slow densification. As it will be discussed in the next section, although not completely avoided, grain growth was very limited during this final stage.

The same principle underpins the protocol of the HP-SPS setup. In this case, the sintering was completed at lower temperature not by extending the dwell to longer holding times, but rather by the application of a higher external pressure (500 MPa instead of 70 MPa). Figure 6 shows the piston relative displacement and piston speed recorded during the heating ramps of the SPS and HP-SPS treatments. The result of the increased applied pressure was the earlier onset of the sintering process (about 100 °C lower, reduced from 350 to 250 °C), that was also accompanied by a lower maximum temperature to reach the target density (decreased of about 300 °C, from 900 to 600 °C).

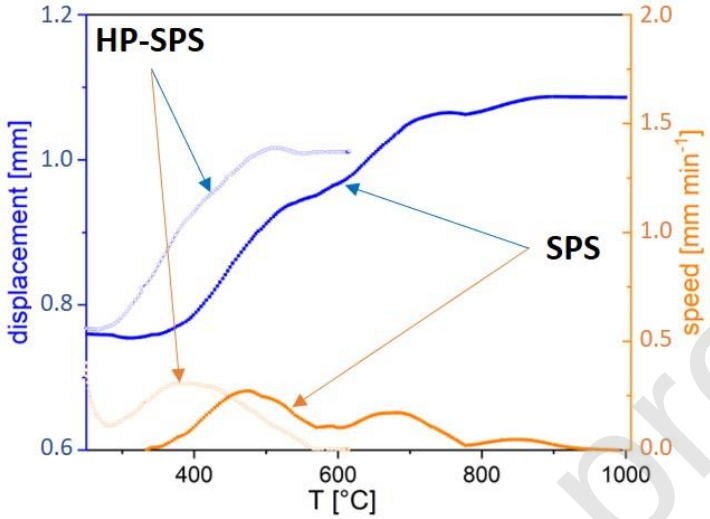

Figure 6: Comparison of the sintering behaviour of UO_2 nanopowders during the SPS and HP-SPS treatments, in terms of piston relative displacement and speed versus temperature. The increase of the applied pressure, from 70 to 500 MPa, shifts the onset (from 350 to 250 °C) and the end (from 900 to 600 °C) of the sintering to lower temperatures. The curve of the HP-SPS piston displacement was translated down to the SPS one to simplify the comparison.

3.3 UO_2 pellets

The microstructures resulting from sintering the UO_2 nanopowders from hydrothermal decomposition of oxalate using SPS (1600 °C), 2S-SPS (650-550 °C), and HP-SPS (660 °C) are presented in Figure 7. The final average grain sizes were respectively 3.08 ± 0.06 µm, 478 ± 17 nm, and 163 ± 9 nm. Contrarily to the HP-SPS and 2S-SPS treatments, the single-step SPS was not optimised for avoiding grain growth. The decrease of the sintering temperature brought by the HP-SPS was enough to hamper the final grain size matching that of the HBS in spent fuel (100-300 nm). In the 2S-SPS, the final grain size remained small, but grain growth was not completely inhibited. This was revealed by the comparison with the microstructure of a sample heated to T_1 = 650 °C and then quenched, displaying a density of 82 % TD and a grain size around 300 nm (not shown here). If the density of triple point junctions was large enough, densification during the dwell at T_2 = 550 °C should have occurred without any grain growth, while in this case it was accompanied by some coarsening.

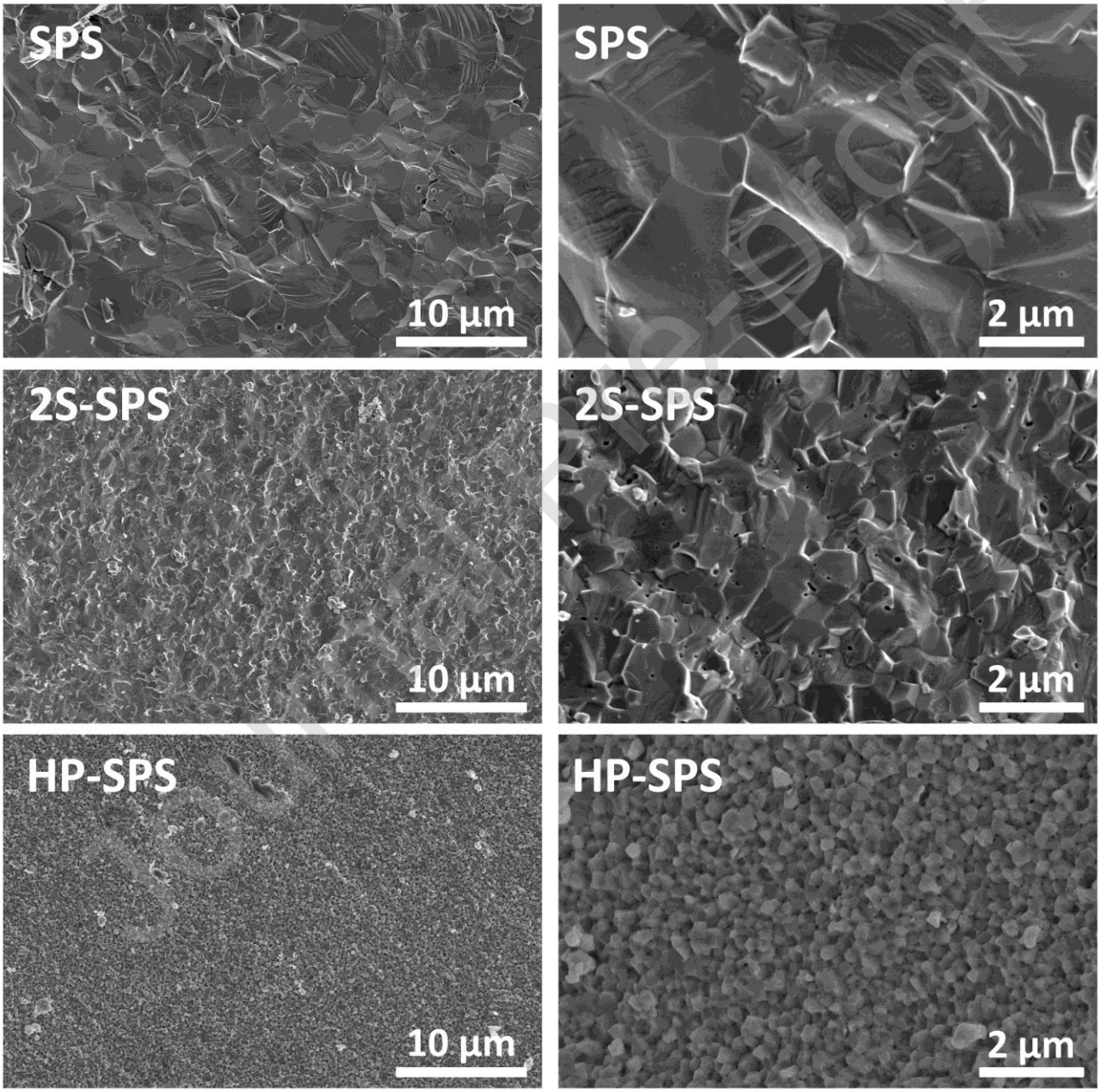

Figure 7: SEM SE pictures of the final microstructures obtained by applying the SPS, 2S-SPS, and HP-SPS treatments to the UO_2 nanopowders.

The lattice parameters obtained from the XRD refinements revealed O/M ratios of 2.00 for SPS and 2S-SPS, and 2.04 for HP-SPS. By performing the reduction treatment at 600 °C during a relatively short time, well below the maximum temperature experienced by the samples during sintering, no significant grain growth took place. The comparison of a sample before and after the annealing presented in Figure 8 shows that the microstructural characteristics were preserved.

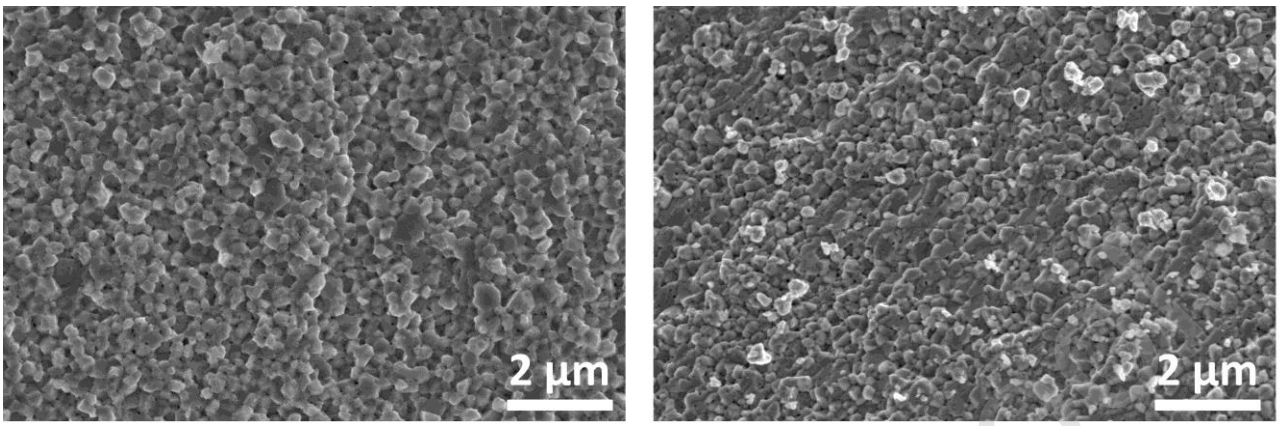

Figure 8: SEM SE images of a HP-SPS disk before (left) and after (right) annealing under Ar-4%H_2 at 600 °C for 2 h. At this temperature, no grain growth occurs.

With the final goal of having a set of identical UO_2 samples differing only by the grain size, also the stoichiometric samples were annealed using the same heating treatment. Figure 9 shows the XRD patterns of the sintered UO_2 disks after the annealing, and the initial nanopowder for comparison. The peak positions of the annealed disks overlap, as the O/M ratio was reduced to 2.00 also for the HP-SPS sample. As the crystallite size exceeds 100 nm in all the disks, no significant difference in the peak FWHM with the XRD can be evidenced using the setup of this work.

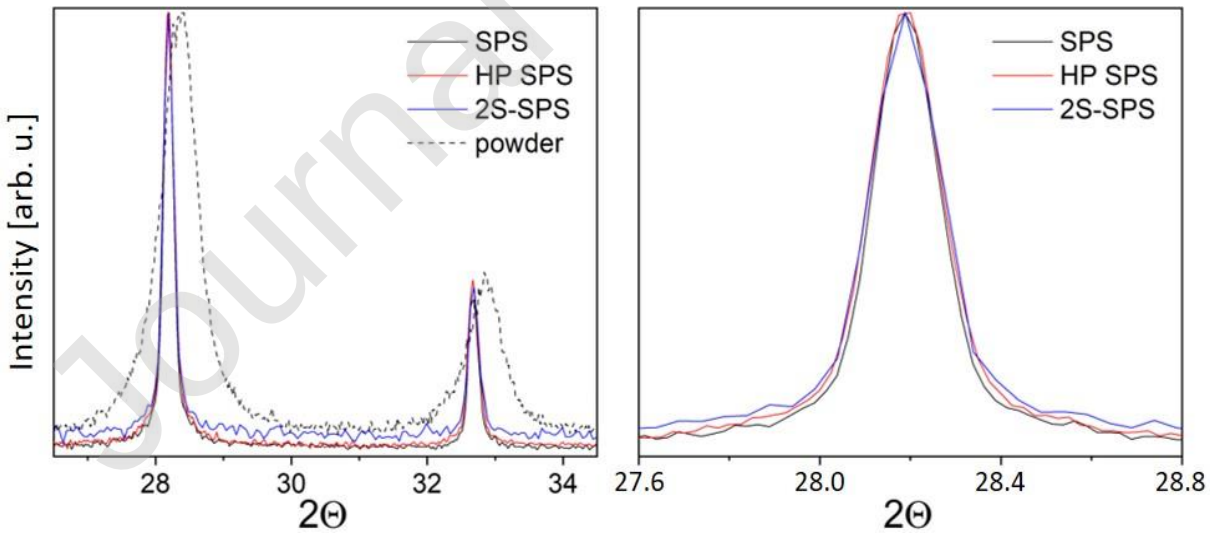

Figure 9: XRD pattern of the UO_2 nanopowder (left) and sintered disks after annealing (right).

As can be seen in Table 3, the microstrain of the in the $UO_{2.04}$ HP-SPS sample was one order of magnitude higher than in the stoichiometric samples. Application of the Williamson – Hall approach showed no dependence of the microstrain on the probed depth (i.e. Bragg angle), meaning that the

lattice parameter variation was between border and centre of the grains. After annealing, the microstrain of all samples was in the same order of magnitude. Complete reduction to $UO_{2.00}$ was thus achieved uniformly throughout the whole depth of the sample, and from the grain surfaces to the centres.

	As sintered		After annealing	
Treatment	O/M	Microstrain [10^{-4}]	O/M	Microstrain [10^{-4}]
SPS	2.00	3	2.00	4
2S-SPS	2.00	4	2.00	3
HP-SPS	2.04	18	2.00	8

Table 3: comparison of the O/M ratios and microstrain as calculated from the XRD data before and after annealing.

A grain size of about 160 nm and the fluorite structure of the HP-SPS sintered material were also confirmed by TEM analyses, such as the picture shown in Figure 10. The selective area electron diffraction pattern (SAED) of Figure 10 has been indexed by a Fm-3m fluorite structure. From the SAED recorded on several areas no texture could be evidenced. The grains are randomly oriented and show high angle grain boundaries (HAGB). No analyses were performed to determine any strain in complement to the XRD characterization that typically would give more accurate results. At such high magnifications, a large amount of nanometric pores have been observed, some of which were partially visible also in SEM pictures. The large concentration of pores was explained by the limited coarsening that accompanied densification in HP-SPS, keeping the average pore size around or below 20 nm (marked by the arrow in Figure 10). As the fractional volume of the porosity was the same among all samples (5 %), the number of pores increased as their size decreased, and they became visible only at higher magnifications. The pores have been excluded to be resulting from the FIB preparation of the TEM lamellae as they are observed on the SEM and in the bulk of the TEM lamellae.

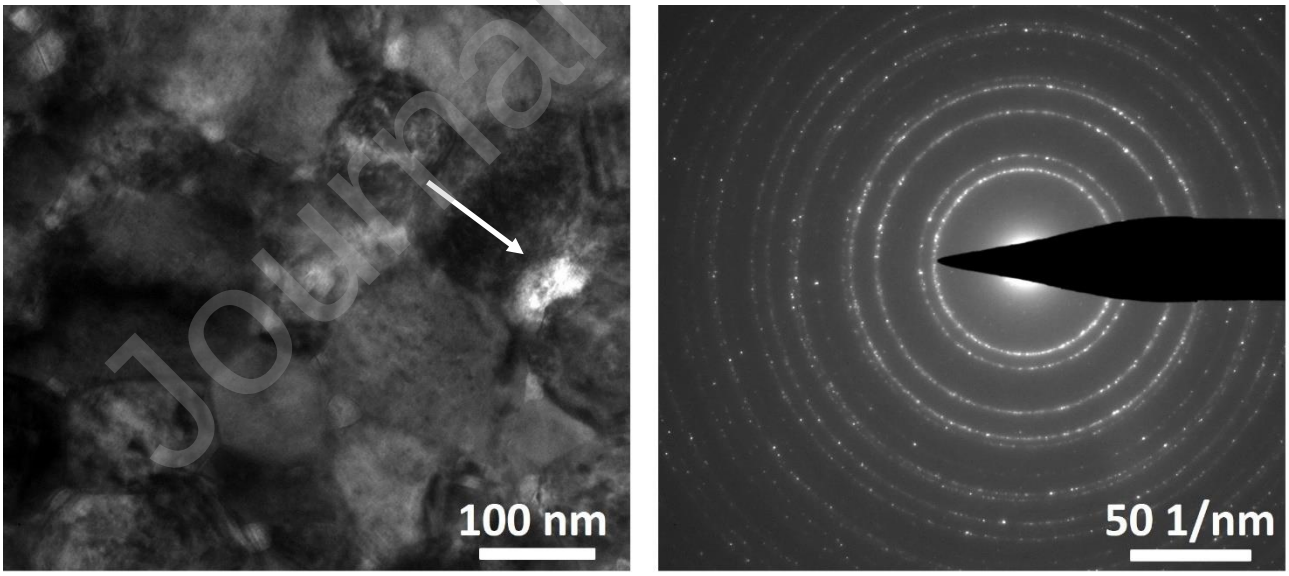

Figure 10: Microstructure and diffraction pattern as obtained by TEM on an HP-SPS UO_2 sample.

3.4 Comparison between different SPS methods

As shown in the previous sections, SPS is a very flexible technique that allows obtaining extremely dissimilar final microstructures by starting from the same material and properly designing the thermal

treatment. In this work, for the first time in UO_2 processing, the two-step sintering technique was combined with SPS, and its outcome was compared to what obtained by single-step SPS and HP-SPS. Each one of these treatments showed some distinct advantages with respect to the others, but none of them was flawless. Table 4 gives an overview of the treatments applied in this work, together with a summary of their final results, and a list of advantages and drawbacks.

Coarsening during sintering was extremely limited in HP-SPS, which led to the smallest final grain size. However, this came with some processing drawbacks. Due to its complexity, the HP setup took more time and effort to assemble (which is an issue especially when working in a glovebox), and decreased the accuracy of the temperature measurement. Moreover, the SiC components were breaking systematically during the treatment, and the final disks also had very low mechanical stability due to the high residual stresses. The use of SiC inserts, combined with the low temperature and time needed, implied a loss of the reducing atmosphere during sintering, leading to hyperstoichiometric final disks when processing non-stoichiometric powders.

In this regard, 2S-SPS has some complementary advantages. Despite the extremely low temperatures, the long hold time and the use of graphite components lead to stoichiometric $UO_{2.00}$ final disks. Remarkably, the combination of low temperature and pressure opens up to the possibility of exploring different die materials for this type of SPS treatment. 2S-SPS however comes with the drawback of an increased hold time (although always considerably shorter than conventional two-step sintering). Coarsening was also to some extent limited during densification, although this approach still needs some adjustments to allow reaching grain size as small as the one of HBS.

It is worth mentioning that two-step conventional free sintering already yields the advantage of limiting significantly coarsening during densification. As reported in the only work found in literature, 95 % TD UO_2 with a final grain size of 0.9 µm was obtained after sintering at 1410-1310 °C for 12 h[29]. The application of the same approach to SPS led to a halving of the final grain size (although the starting powder was not the same), at much lower sintering temperatures and hold times.

	Single-step SPS	**2S- SPS**	**HP-SPS**
Temperature	1600 °C	650-550 °C	660 °C
Pressure	70 MPa	70 MPa	500 MPa
Time	10 min	100 min	0.5 min
Final grain size	3.08 ± 0.06 µm	478 ± 17 nm	163 ± 9 nm
Final O/M	2.00	2.00	2.04
Setup	Regular (simple)	Regular (simple)	HP setup (complex)
Residual stress	Low	Low	High (low mechanical stability)
Advantages	+ Quick sintering + Simple setup + Excellent final stoichiometry	+ Simple setup + Low T + Low pressure + Excellent final stoichiometry + Small final grain size	+ Very fast sintering + Low T + Smallest final grain size

Drawbacks	- Coarse final microstructure	- Long sintering time	- Complex setup (long installation, lower T measurement accuracy) - SiC components break systematically - Deviation from stoichiometry - High residual stress (disks tend to break while handling)

Table 4: comparison of the sintering parameters, final outcomes, advantages, and drawbacks of the SPS methods used.

4 Summary and conclusions

Single-step Spark Plasma Sintering (SPS), High-Pressure SPS (HP-SPS), and, for the first time, two-step SPS (2S-SPS), were used to sinter near-stoichiometric nanocrystalline UO_{2+x} powders into dense (95 % TD) UO_2 disks. The nanopowders were produced either by thermal or hydrothermal decomposition of U(IV) oxalate, at 600°C and 170°C, respectively. The hydrothermally decomposed powders had a crystallite size of 5 nm. The oxalate stacked-platelets structure typical of the simple heat treatment (thermal decomposition) was completely disassembled thanks to the autogenic pressure, resulting into highly sinteractive powders. The sintering onset and end were shifted to lower temperatures by 70 and 250 °C respectively, in comparison with UO_2 nanopowders of comparable crystallite size obtained through the thermal route. As a drawback, these powders were prone to quick oxidation, even in the glovebox under Ar atmosphere. Due to the lack of the reductive graphite environment, HP-SPS was not able to fully reduce the powders to $UO_{2.00}$ during sintering, and thus a further reduction treatment of 2 h at 600 °C under Ar-H_2 was required.

HP-SPS and 2S-SPS treatments were optimised to control coarsening during densification of the powders by limiting the maximum sintering temperatures. Stoichiometric, dense (95 % TD) UO_2, with 478 ± 17 nm of average grain size, was sintered in 2S-SPS at temperatures as low as 650-550 °C (70 MPa, 3 s and 100 min hold times). Slightly hyperstoichiometric 95 % TD $UO_{2.04}$ disks of 163 ± 9 nm of grain size were obtained by HP-SPS at 660 °C (500 MPa, 30 s hold time). A non-optimised single-step SPS run at 1600 °C (70 MPa, 10 min hold time) yielded 95 % TD dense $UO_{2.00}$ with 3.08 ± 0.06 µm grain size. A set of samples differing by their grain size was obtained after an annealing to homogenise all stoichiometries to $UO_{2.00}$. Intermediate grain sizes can be obtained by increasing the temperatures or hold times during sintering, or by applying further thermal treatments at temperatures higher than the sintering one to trigger grain growth. Such set of samples is suitable for separate effect studies on the importance of grain boundaries in UO_2, like on gas diffusion or defect mobility.

Declaration of interests

The authors declare that they have no known competing financial interests or personal relationships that could have appeared to influence the work reported in this paper.

5 Acknowledgement

This work was funded by the European Commission and performed at the European Commission Joint Research Centre in Karlsruhe (Germany).

References

1. Klein, D., Baer, W. & Smith, G. G. Spatial Distribution of U^{238} Resonance Neutron Capture in Uranium Metal Rods. *Nucl. Sci. Eng.* **3**, 698–706 (1958).

2. Noirot, J., Desgranges, L. & Lamontagne, J. Detailed characterisations of high burn-up structures in oxide fuels. *J. Nucl. Mater.* **372**, 318–339 (2008).

3. Rondinella, V. V. & Wiss, T. The high burn-up structure in nuclear fuel. *Mater. Today* **13**, 24–32 (2010).

4. Sonoda, T. *et al.* Transmission electron microscopy observation on irradiation-induced microstructural evolution in high burn-up UO_2 disk fuel. *Nucl. Instruments Methods Phys. Res. Sect. B Beam Interact. with Mater. Atoms* **191**, 622–628 (2002).

5. Wiss, T. *et al.* Recent Results of Microstructural Characterization of Irradiated Light Water Reactor Fuels using Scanning and Transmission Electron Microscopy. *JOM* **64**, 1390–1395 (2012).

6. Wiss, T. *et al.* Properties of the high burnup structure in nuclear light water reactor fuel. *Radiochim. Acta* **105**, 893–906 (2017).

7. Ronchi, C., Sheindlin, M., Staicu, D. & Kinoshita, M. Effect of burn-up on the thermal conductivity of uranium dioxide up to 100.000 MWdt-1. *J. Nucl. Mater.* **327**, 58–76 (2004).

8. Manzel, R. & Walker, C. . EPMA and SEM of fuel samples from PWR rods with an average burn-up of around 100 MWd/kgHM. *J. Nucl. Mater.* **301**, 170–182 (2002).

9. Lucuta, P. G., Matzke, H., Verrall, R. A. & Tasman, H. A. Thermal conductivity of SIMFUEL. *J. Nucl. Mater.* **188**, 198–204 (1992).

10. Matzke, H., Lucuta, P. G., Verrall, R. A. & Henderson, J. Specific heat of UO_2-based SIMFUEL. *J. Nucl. Mater.* **247**, 121–126 (1997).

11. Oversby, V. M. M. *Uranium dioxide, SIMFUEL, and spent fuel dissolution rates - a review of published data*. (1999).

12. Cacuci, D. G. *Handbook of Nuclear Engineering*. *Springer* (Springer US, 2010). doi:10.1007/978-0-387-98149-9

13. Kok, K. D. *Nuclear Engineering Handbook*. (CRC Press, 2009). doi:10.1201/9781420053913

14. Ge, L., Subhash, G., Baney, R. H. & Tulenko, J. S. Influence of processing parameters on thermal conductivity of uranium dioxide pellets prepared by spark plasma sintering. *J. Eur. Ceram. Soc.* **34**, 1791–1801 (2014).

15. Chen, Z., Subhash, G. & Tulenko, J. S. Master sintering curves for UO_2 and UO_2–SiC composite processed by spark plasma sintering. *J. Nucl. Mater.* **454**, 427–433 (2014).

16. Wangle, T., Tyrpekl, V., Cologna, M. & Somers, J. Simulated UO_2 fuel containing CsI by spark plasma sintering. *J. Nucl. Mater.* **466**, 150–153 (2015).

17. Le Gall, C. Contribution to the study of fission products release from nuclear fuels in severe accident conditions: effect of the pO_2 on Cs, Mo and Ba speciation. (2018).

18. Cologna, M., Tyrpekl, V., Ernstberger, M., Stohr, S. & Somers, J. Sub-micrometre grained UO_2 pellets consolidated from sol gel beads using spark plasma sintering (SPS). *Ceram. Int.* **42**, 6619–6623 (2016).

19. Tyrpekl, V. *et al.* Preparation of bulk-nanostructured UO_2 pellets using high-pressure spark plasma sintering for LWR fuel safety assessment. *J. Am. Ceram. Soc.* **100**, 1269–1274 (2017).

20. Yao, T., Scott, S. M., Xin, G., Gong, B. & Lian, J. Dense nanocrystalline UO_{2+x} fuel pellets synthesized by high pressure spark plasma sintering. *J. Am. Ceram. Soc.* **101**, 1105–1115 (2018).

21. Yao, T. *et al.* Grain growth and pore coarsening in dense nano-crystalline UO_{2+x} fuel pellets. *J. Am. Ceram. Soc.* **100**, 2651–2658 (2017).

22. Gong, B. *et al.* Nano- and micro-indentation testing of sintered UO_2 fuel pellets with controlled microstructure and stoichiometry. *J. Nucl. Mater.* **516**, 169–177 (2019).

23. De Bona, E. *et al.* Synthesis of nanostructured ThO_2 pellets. *J. Am. Ceram. Soc.* **102**, 3814–3818 (2019).

24. Chen, I.-W. & Wang, X.-H. Sintering dense nanocrystalline ceramics without final-stage grain growth. *Nature* **404**, 168–171 (2000).

25. Razavi Hesabi, Z., Haghighatzadeh, M., Mazaheri, M., Galusek, D. & Sadrnezhaad, S. K. Suppression of grain growth in sub-micrometer alumina via two-step sintering method. *J. Eur. Ceram. Soc.* **29**, 1371–1377 (2009).

26. Mazaheri, M., Valefi, M., Hesabi, Z. R. & Sadrnezhaad, S. K. Two-step sintering of nanocrystalline $8Y_2O_3$ stabilized ZrO_2 synthesized by glycine nitrate process. *Ceram. Int.* **35**, 13–20 (2009).

27. Mazaheri, M., Simchi, A. & Golestani-Fard, F. Densification and grain growth of nanocrystalline 3Y-TZP during two-step sintering. *J. Eur. Ceram. Soc.* **28**, 2933–2939 (2008).

28. Wang, C.-J., Huang, C.-Y. & Wu, Y.-C. Two-step sintering of fine alumina–zirconia ceramics. *Ceram. Int.* **35**, 1467–1472 (2009).

29. Vidal, J., Zemek, M. & Blanchart, P. Densification of UO_2 via Two Step Sintering. in *Advances in Sintering Science and Technology II* 173–184 (2012). doi:10.1002/9781118486955.ch15

30. Li, B., Liu, D., Liu, J., Hou, S. & Yang, Z. Two-step sintering assisted consolidation of bulk titania nano-ceramics by spark plasma sintering. *Ceram. Int.* **38**, 3693–3699 (2012).

31. Schwarz, S. & Guillon, O. Two step sintering of cubic yttria stabilized zirconia using Field Assisted Sintering Technique/Spark Plasma Sintering. *J. Eur. Ceram. Soc.* **33**, 637–641 (2013).

32. Tyrpekl, V. *et al.* Low temperature decomposition of U(IV) and Th(IV) oxalates to nanograined oxide powders. *J. Nucl. Mater.* **460**, 200–208 (2015).

33. Martinez, J. *et al.* From uranium(IV) oxalate to sintered UO_2 : Consequences of the powders' thermal history on the microstructure. *J. Eur. Ceram. Soc.* **35**, 4535–4546 (2015).

34. Tyrpekl, V., Cologna, M., Robba, D. & Somers, J. Sintering behaviour of nanocrystalline ThO_2 powder using spark plasma sintering. *J. Eur. Ceram. Soc.* **36**, 767–772 (2016).

35. Wangle, T. *et al.* Morphology dependent sintering path of nanocrystalline ThO_2. *J. Nucl. Mater.* **533**, 152081 (2020).

36. Walter, O., Popa, K. & Blanco, O. D. Hydrothermal decomposition of actinide(IV) oxalates: a new aqueous route towards reactive actinide oxide nanocrystals. *Open Chem.* **14**, (2016).

37. Popa, K. *et al.* A low-temperature synthesis method for AnO_2 nanocrystals (An = Th, U, Np, and Pu) and associate solid solutions. *CrystEngComm* **20**, 4614–4622 (2018).

38. Balice, L. *et al.* Nano and micro U_{1-x} Th_x O_2 solid solutions: From powders to pellets. *J. Nucl. Mater.* **498**, 307–313 (2018).

39. Manaud, J. *et al.* Hydrothermal Conversion of Uranium(IV) Oxalate into Oxides: A Comprehensive Study. *Inorg. Chem.* **59**, 3260–3273 (2020).

40. Lucuta, P. G., Matzke, H. & Hastings, I. J. A pragmatic approach to modelling thermal conductivity of irradiated UO_2 fuel: Review and recommendations. *J. Nucl. Mater.* **232**, 166–180 (1996).

41. Guéneau, C., Chartier, A. & Van Brutzel, L. Thermodynamic and Thermophysical Properties of the Actinide Oxides. in *Comprehensive Nuclear Materials* 21–59 (Elsevier, 2012). doi:10.1016/B978-0-08-056033-5.00009-4

42. Olander, D. R. *Fundamental aspects of nuclear reactor fuel elements*. (1976). doi:10.2172/7343826

43. Franceschin, G., Flores-Martínez, N., Victorio, G. V., Ammar, S. & Valenzuela, R. Sintering and Reactive Sintering by Spark Plasma Sintering (SPS). in *Sintering of Functional Materials* (InTech, 2018). doi:10.5772/intechopen.68871

44. Tyrpekl, V. *et al.* Implementation of a spark plasma sintering facility in a hermetic glovebox for compaction of toxic, radiotoxic, and air sensitive materials. *Rev. Sci. Instrum.* **86**, 023904 (2015).

45. Petříček, V., Dušek, M. & Palatinus, L. Crystallographic Computing System JANA2006: General features. *Zeitschrift für Krist. - Cryst. Mater.* **229**, 345 (2014).

46. Teske, K., Ullmann, H. & Rettig, D. Investigation of the oxygen activity of oxide fuels and fuel-fission product systems by solid electrolyte techniques. Part I: Qualification and limitations of the method. *J. Nucl. Mater.* **116**, 260–266 (1983).

47. Williamson, G. . & Hall, W. . X-ray line broadening from filed aluminium and wolfram. *Acta Metall.* **1**, 22–31 (1953).

48. E112-12. Standard Test Methods for Determining Average Grain Size. *ASTM Int.* **E112**-**12**, 1–27 (2012).

49. Lábár, J. L. Consistent indexing of a (set of) single crystal SAED pattern(s) with the ProcessDiffraction program. *Ultramicroscopy* **103**, 237–249 (2005).

50. Belbeoch, B., Boivineau, J. C. & Perio, P. Changements de structure de l'oxyde U_4O_9. *J. Phys. Chem. Solids* **28**, 1267–1275 (1967).

51. Matzke, H. On uranium self-diffusion in UO_2 and UO_{2+x}. *J. Nucl. Mater.* **30**, 26–35 (1969).

52. Yan, M. F. Microstructural control in the processing of electronic ceramics. *Mater. Sci. Eng.* **48**, 53–72 (1981).